Microstructure technology for fabrication of metal-mesh grids

Milton Rebbert, Peter Isaacson, Jacqueline Fischer, Matthew A. Greenhouse, Julius Grossman, Martin Peckerar, and Howard A. Smith

Motivated by the need for highly efficient far-IR Fabry–Perot étalons for airborne and space astronomy, we have developed a high-yield photolithographic technique for producing low-loss metal-mesh reflectors. We describe the production technique and report on the mesh flatness and uniformity. Optical measurements of meshes produced by this technique show that absorptivity of less than 1% with reflectivity of more than 98% was achieved at the longest wavelengths measured, which proved them to be significantly more efficient than commercially available meshes. This process can achieve wire widths that are less than the mesh thicknesses (typically 3 μm), which extends their applicability to wavelengths as short as ~20 μm without sacrificing mechanical strength for airborne and space-flight applications.

Key words: Fabry–Perot, far-infrared, metal mesh, microstructure technology.

1. Introduction

Metal grids used as low-absorption, partially transmitting reflectors are needed for a variety of applications in optics. The requirements are most stringent for use in Fabry–Perot[1] étalons for spectroscopy. Fabry–Perot étalons take advantage of interference effects that are produced by radiation that has undergone multiple reflections, as described by the Airy formula for two parallel reflectors. They therefore require flat, high-reflectivity plates with low absorption. The reflective surfaces of étalons that operate in the visible can be dielectric coatings or thin metal films. In the far IR ($\lambda > 30$ μm) dielectric coatings are impractical for several reasons. Since they are composed of multiple layers of quarter-wave and half-wave thicknesses, they tend to separate, particularly when cycled to the cryogenic temperatures necessary for far-IR applications. Also, there are few deposition materials available with the variety of far-IR indices of refraction necessary for broadband high-reflectivity plates. On the other hand, thin metallic films have high absorption for a given reflectivity in the IR,[2] as fixed by the impedance of the metal. In contrast, freestanding metallic meshes, known as inductive metal meshes, can have low absorptivity and still have high reflectivity, because the absorptivity in some metals can be very small, while the reflectivity of the mesh is determined by its geometry.[3] A review of theoretical and experimental work on the IR properties of metal meshes can be found in Sakai and Genzel.[4]

The absorptive properties of the mesh are determined within a skin depth of the surface. Therefore the surface-metal composition, its oxidation, and rms surface roughness decrease the conductivity and thus the transmission of the mesh. In addition to the stringent constraints on the absorption, the Airy formula for the transmission of two plane-parallel reflectors implies that the interference maxima with the highest transmission occur only when the reflectance of both reflectors is identical. Thus one needs precision and accuracy in the fabrication process to produce meshes with equal and uniform reflectivity to obtain high transmission when used as elements of a Fabry–Perot interferometer.

We describe a new fabrication technique developed for mass production of high-precision metal-mesh reflectors. The mesh reflectors produced by this new process have application in space instruments such as the Infrared Space Observatory (ISO) short-wavelength and long-wavelength spectrometers,[5,6] suborbital instruments such as those used on NASA's

M. A. Greenhouse and H. A. Smith are with the Laboratory for Astrophysics, National Air and Space Museum, Smithsonian Institution, Washington, D.C. 20560. J. Grossman is with Sachs/Freeman Associates, Inc., 1401 McCormick Drive, Landover, Maryland 20785. The other authors are with the Naval Research Laboratory, Washington, D.C. 20375; M. Rebbert, P. Isaacson, and M. Peckerar are with the Electronics Science and Technology Division, Code 6804, and J. Fischer is with the Remote Sensing Division, Code 7213.

Received 28 August 1992; revised manuscript received 24 March 1993.

Report Documentation Page

Form Approved
OMB No. 0704-0188

1. REPORT DATE	2. REPORT TYPE	3. DATES COVERED
1994		**00-00-1994 to 00-00-1994**

4. TITLE AND SUBTITLE	5a. CONTRACT NUMBER
Microstructure technology for fabrication of metal-mesh grids	5b. GRANT NUMBER
	5c. PROGRAM ELEMENT NUMBER
6. AUTHOR(S)	5d. PROJECT NUMBER
	5e. TASK NUMBER
	5f. WORK UNIT NUMBER
7. PERFORMING ORGANIZATION NAME(S) AND ADDRESS(ES) **Naval Research Laboratory,4555 Overlook Avenue, SW,Washington,DC,20375**	8. PERFORMING ORGANIZATION REPORT NUMBER
9. SPONSORING/MONITORING AGENCY NAME(S) AND ADDRESS(ES)	10. SPONSOR/MONITOR'S ACRONYM(S)
	11. SPONSOR/MONITOR'S REPORT NUMBER(S)

12. DISTRIBUTION/AVAILABILITY STATEMENT
Approved for public release; distribution unlimited

13. SUPPLEMENTARY NOTES

14. ABSTRACT

15. SUBJECT TERMS

16. SECURITY CLASSIFICATION OF:			17. LIMITATION OF ABSTRACT	18. NUMBER OF PAGES	19a. NAME OF RESPONSIBLE PERSON
a. REPORT **unclassified**	b. ABSTRACT **unclassified**	c. THIS PAGE **unclassified**		**7**	

Kuiper Airborne Observatory, and other systems now being planned. The meshes can also be made into high-efficiency narrowband filters and polarizers for a variety of IR instruments. Laboratory tests described by Greenhouse *et al.*[7] show that the mesh reflectors produced by this program define the state of the art for low-absorption, high-reflectivity, metal-mesh Fabry–Perot étalons.

These optical applications place stringent demands on fabrication processes. The mesh wire width, periodicity, and thickness must be uniform over a large area, and the rms surface roughness of the mesh must be low for high transmission (30 nm at $\lambda = 50$ μm). The reflective surface should be inert and have the highest possible conductivity at the operating temperature of the mesh. The mesh structure must be durable so that it can be stretched into flat plane reflectors and withstand repeated cycles to cryogenic temperatures.

A patented process for producing meshes that satisfy these requirements is described by Taylor *et al.*[8] Our purpose was to improve the process in order (1) to fabricate wire widths as narrow as 2 μm for Fabry–Perot reflectors for IR wavelengths as short as 20 μm, (2) to improve the conductivity of the front surface and the smoothness of the sidewalls, and (3) to adapt the process for batch processing on a production line by reduction of the number and complexity of the processing steps. While a number of salient process changes were made, the main difference between this process and the Taylor process is the use of a template plating metallization process instead of a lift-off process. This new approach adds more versatility to the process because the final wire width is independent of the final mesh thickness. The front surface of the mesh is pure gold for improved conductivity, and the sidewalls are steep and smooth. This new method also significantly improves the yield of space-qualifiable meshes to ~30%.

2. Process Description

A. Summary

Various metals were considered as mesh materials, among them were copper, gold, gold-coated copper, nickel, and gold-coated nickel. Gold-coated nickel was chosen because nickel has the required rigidity and elastic modulus, while gold has high reflectance because of its conductivity and inert properties. Starting with a stock silicon wafer that is coated with gold, we used a photolithographic process to produce a pattern in a thick photoresist on the wafer. This photoresist pattern was used as a template for the metal up-plating of the mesh structure. The silicon wafer was etched away, and we removed the thin gold plating base left in the aperture by ion milling, leaving a free-standing metal mesh, with a rectangular wire cross section and sharp corners, stretched across a silicon support ring (Fig. 1). The gold front surface of this mesh retained the original flatness of the polished silicon wafer.

In detail the process can be divided into four steps:

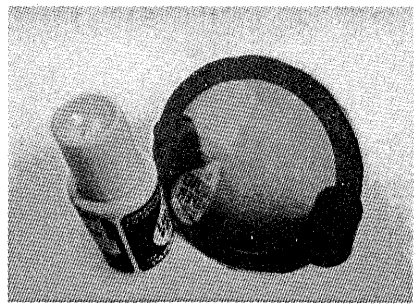

Fig. 1. Typical freestanding mesh. The mesh is supported by an annular ring of the original silicon wafer substrate. Reflection as well as transmission is seen, which illustrates the smoothness of the mesh surface.

wafer preparation, pattern formation, silicon etching, and mesh finishing. We describe each subprocess in detail below.

B. Wafer Preparation

The starting material, a 76-mm-diameter, *N*-type, 4–9-Ω cm, ⟨100⟩-oriented silicon wafer, was cleaned with a hydrogen peroxide cleaning solution.[9] A thermal oxide was then grown to a thickness of 20 nm on both sides of the wafer [Fig. 2(a)] to promote adhesion for subsequent metal-film depositions.

Chrome and gold films were deposited on both sides of the wafer. On the front side the metal covered the entire surface to provide an active cathode surface for the nickel electroplating. On the back side of the wafer the metal was deposited in an annular pattern with the center of the wafer clear of metal and the metal ring extending to the edge of the wafer [Fig. 2(b)]. This back-side ring formed the basis of the etch mask for the silicon etch step. The 5–10-nm-thick chrome film promoted adhesion of the gold film. A gold film of 100-nm thickness ensured good electrical conduction during the plating step. By diffusion these layers formed a chrome–gold film.

The metal films were deposited at a pressure of 10^{-5} Pa. The chrome was deposited by a resistively heated chrome-plated tungsten rod. This method obtained good control of the deposition without spitting at low evaporation rates (0.5 nm/s). The gold was evaporated from an aluminum-coated molybdenum crucible at a rate of 2 nm/s. The back and front of the wafer were metallized in subsequent steps. An aluminum disk 52 mm in diameter masked off the center of the wafer during the metal deposition. Previously[8] a lithographic lift-off[10] procedure masked the wafer's back side. This procedure required an additional cleaning step and had the potential for contaminating the vacuum system with out-gassing solvents from the photoresist.

C. Pattern Formation

We fabricated several mesh geometries, all with a 52-mm clear aperture and 3-μm wire thickness. The wire widths and periods are listed in Table 1.

To form the pattern, we considered both subtractive and additive processes. In a subtractive process

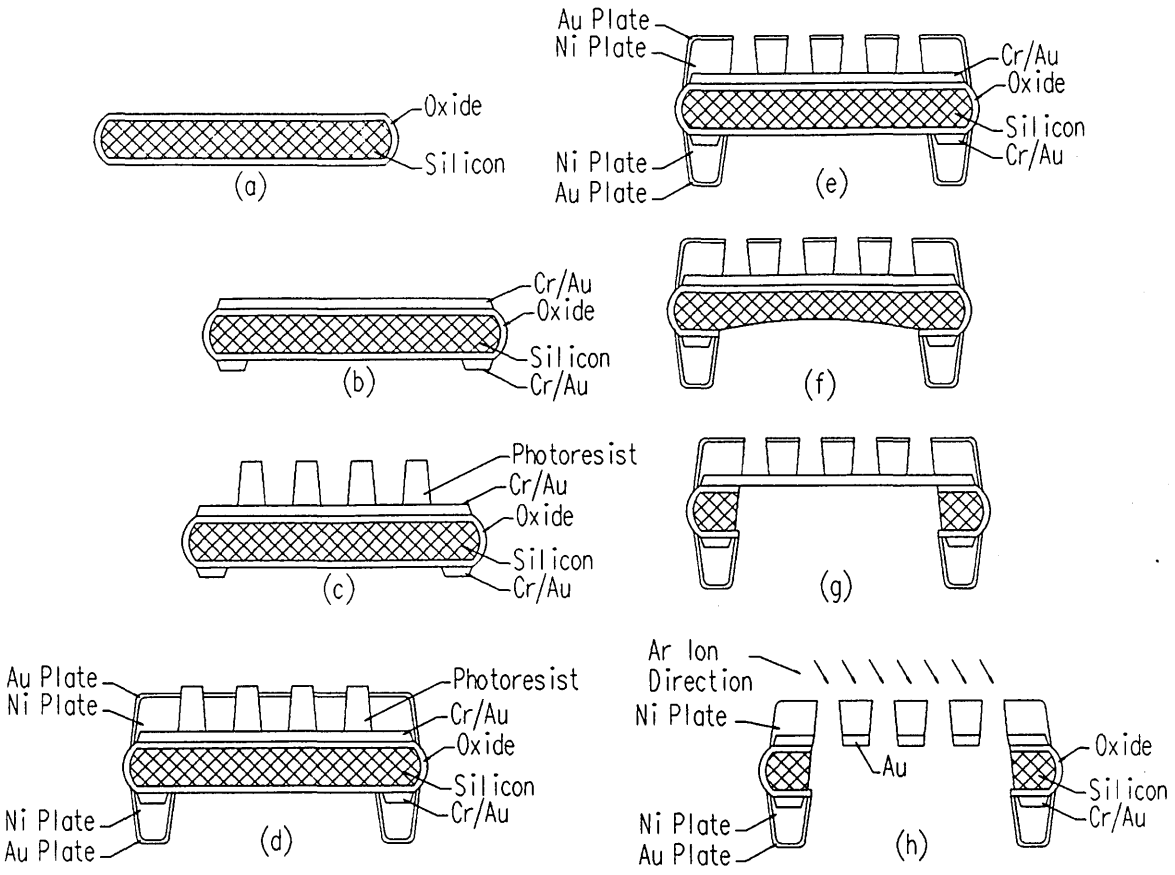

Fig. 2. Fabrication steps: (a) A thermal oxide is grown on both sides of the wafer. (b) A chrome–gold film is deposited over the oxide on both sides of the wafer. (c) A layer of photoresist is deposited, exposed through a mask, and developed. The sidewall angle is greatly exaggerated for clarity. (d) Nickel is up-plated by the resist template to form nearly perpendicular sidewalls. (e) The resist template is removed, leaving a nickel mesh on a gold film, all on a silicon wafer. (f) The back side of the silicon wafer is thinned from the center to the edge, putting a dimple in the back side of the wafer. (g) The silicon, chrome, and oxide are etched away, leaving a full gold membrane and nickel mesh. (h) Ion milling is used to mill the gold membrane between the nickel wires, from the back side of the mesh, leaving a smooth, gold coating on the front side of the freestanding mesh.

a film of the desired thickness is deposited on the substrate. A pattern of a resist material is formed on top of the film by photolithographic methods. The areas not covered by resist are etched away (subtracted) with an appropriate chemical etch. The resist material is removed, leaving behind the desired pattern. In an additive process a template is formed in resist by a photolithographic method and the desired film is deposited in the exposed regions of the substrate. The resist template is removed, leaving behind the desired pattern. The wet etching used in the former process yields a wall angle of 45 deg, whereas a sidewall angle near 90° was desired. This drawback could in principle be alleviated by dry etching, such as reactive ion etching or ion milling,[11] if a suitable etch differential between the mask

Table 1. Mesh Uniformity and Sample-to-Sample Variation Measurements

Design Parameters		Mask Measurements				Metal Mesh Measurements						
Linewidth (μm)	Period (μm)	Linewidth (μm)[a]	Uniformity s.d. (μm)	Period (μm)[b]	Uniformity s.d. (μm)	Linewidth (μm)[c]	Uniformity s.d. (μm)	Sample to Sample s.d. (μm)	Period (μm)[d]	Uniformity s.d. (μm)	Sample to Sample s.d. (μm)	Number of Meshes Measured
2.5	10.0	2.29	0.18	10.04	0.17	2.69	0.23	0.49	10.02	0.15	0.08	40
6.0	15.5	5.24	0.12	15.57	0.11	5.92	0.16	0.39	15.58	0.12	0.06	74
6.0	19.0	5.57	0.17	19.04	0.11	6.18	0.18	0.39	19.08	0.13	0.09	66

[a]Based on 50 measurements/mask.
[b]Based on 25 measurements/mask.
[c]Based on 10 measurements/mesh.
[d]Based on 5 measurements/mesh.

material and the nickel mesh could be found and the redeposition of material on the wafer during the etch could be controlled.

We ultimately chose an additive process in which the template is formed on the front side of the gold by a photolithographic processing scheme that is common in the manufacturing of semiconductor circuits. With this approach a collimated beam of UV light projects a mask pattern onto a substrate that is coated with a UV-sensitive photoresist. The mask blocks the light from certain areas of the substrate while unmasked areas are exposed. On chemical development of the exposed substrate, the resist material in exposed regions is removed, leaving behind the resist in the unexposed regions.

The complete lithographic process is complex. The layout of the pattern for the mask was accomplished with a computer-aided-design software package. The computer-aided-design data were then down loaded to a Cambridge EBMF-6 electron-beam lithography machine. This mask-making step used a subtractive processing sequence to expose a resist that covered a chrome film (80 nm) on a glass plate (the mask material). The resist pattern was then developed, and the chrome was etched away in the unprotected areas. The resist was stripped away, leaving the desired chrome pattern on a glass plate to be used as a production mask.

The mask was then placed in the Karl Süss MJB-3 contact exposure tool. This tool has a mercury arc lamp as the UV light source and appropriate optics that produce a collimated beam that projects the mask pattern onto the wafer surface. The wafer was coated with a 4-μm layer of Hoechst AZ-4400 photoresist. After exposure and development of the resist, a resist template 4 μm thick and a sidewall angle of greater than 80 deg remained [Fig. 2(c)].

Next the wafer was placed in a nickel-plating bath. To increase plating uniformity and wafer throughput, a large plating tank was used. As many as 15 wafers at a time were processed in a 1-m^3 tank that held a 600:1 mixture of ACR 3008 nickel-plating solution.

The plating process was run at 55 °C. The time and current varied with the number of wafers plated at one time. A typical run contained six wafers and was followed by a rinse and a thin gold plate of 70 nm on top of the nickel [Fig. 2(d)] to protect the nickel from oxidation between processing steps. A cyanide-based plating solution, Sel Rex Aurobond, was used at 50 °C for the gold plating. In this way we could plate additional nickel if needed without removing an oxide layer. The nickel thickness was measured with the stylus step Sloan Dek-Tak I measuring instrument. We took measurements at two points on the plated annulus, using positions that had been covered with clips during plating for reference. After the correct nickel thickness was attained, the resist template was removed to a warm acetone bath. This step left a nickel mesh on a gold film, all on a silicon wafer [Fig. 2(e)].

Taylor *et al.*[8] used a lift-off technique for the mesh pattern formation. This approach had two limitations. In a lift-off process there is no template to guide the buildup of plated metal, so that the wire grows in width and thickness as plating proceeds. This process also produces a reflecting surface with a nonuniform composition and electrical characteristics. In the current process the resist plating guide confines the structures, preserves the sidewall profile, and permits critical dimension control. With this new technique we can achieve linewidths smaller than the mesh thickness, extending the applicability of the reflectors to wavelengths as short as 20 μm.

D. Silicon Etching

In this process step the center of the silicon wafer is etched away from the back-side, leaving a freestanding metal membrane supported on a silicon ring. A 4-*N* (KOH) bath at 80 °C etches the silicon. The metal ring on the back side of the wafer provides an effective etch barrier to the KOH. Before the wafer was placed in the KOH bath, the back side of the silicon wafer was thinned from the center to the edge with a fast silicon etch composed of 4 parts of hydrofluoric acid to 1 part of nitric acid. This technique puts a dimple in the back side of the wafer so that erosion of the silicon during the subsequent KOH etch proceeded reliably from the center to the ring [Fig. 2(f)]. This approach was found to reduce stress and tearing of the membrane during the etch step, resulting in increased yield. Keeping the gold membrane in place during the silicon etch was a key factor in reducing mesh tearing during the KOH etch step. The evaporated gold prevents oxidation of the front mesh surface and also retains the mirror-smooth finish of the polished silicon wafer, which is a significant modification and improvement of the Taylor process.

E. Mesh Finishing

At this point the process has produced a nickel mesh on a freestanding gold membrane that is supported by a silicon ring [Fig. 2(g)]. The membrane is mostly gold but contains some chrome from the adhesion layer and occasionally some silicon oxide from the initial oxidation or chrome oxide that may have developed during the process by diffusion between the latter two layers. The silicon oxide was removed with a 1-min etch in a buffered hydrofluoric acid solution. After a water rinse the chrome or chrome oxide was removed with a 3-min etch in a saturated potassium ferricyanide solution at 50 °C.

To remove the gold from the holes in the mesh, we tried two techniques. In the first technique we assumed that the flatness from the wafer surface would be transferred through the evaporated chrome–gold films to the nickel-plated film. All the gold was removed from the nickel mesh to clear the square holes between the wires; then the nickel mesh was replated with a thin gold layer. The gold film was etched away with a commercial gold etch known as

Metek. The proprietary formula was mixed with water and heated to 50 °C. A 1-min etch removed the gold membrane. After a water rinse the nickel mesh was replated to a thickness of ~70 nm of gold. These meshes proved to be quite suitable Fabry–Perot interferometer elements. However, the reflective surface was rougher than the reflected surface produced by the Taylor process, because the gold etch also attacked the underlying nickel surface.

The second technique for removal of the membrane employed an ion-milling process. With this process a collimated beam of high-energy ions bombards a target, dislodging target atoms and milling away the target material. The nickel mesh on the gold membrane was placed in the ion-milling apparatus so that the beam was directed at the back (nonreflective side) of the mesh [Fig. 2(h)]. The nickel wires became the mask for the milling of the gold membrane. The gold in the hole regions of the mesh was exposed to the milling beam and was milled away, which left behind a smooth gold film on the part of the mesh structure that was masked by the nickel (Fig. 3). By using a beam inclination angle of ~30° and rotating the wafer, we produced smooth sidewalls and a minimum residual gold membrane. The original smoothness of the evaporated gold layer, imparted by the polished substrate wafer, was retained since it was exposed only to dielectric solvents. A side effect of this process is that the back-surface gold is also removed. This removal would not appear to have a significant effect on the transmission or finesse of a Fabry–Perot étalon, since the multiple reflections primarily involve the front surface and the sidewalls. It is difficult to gold plate the sidewalls at this stage, because the nickel surface is quickly oxidized.

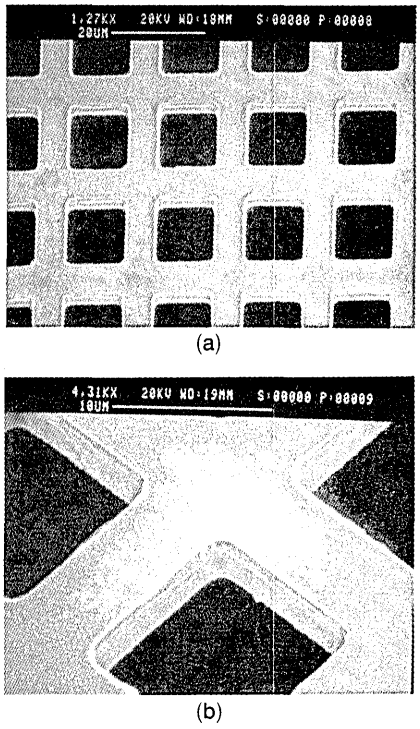

(a)

(b)

Fig. 3. Scanning electron micrographs of the front surfaces of typical freestanding meshes at (a) low magnification and (b) high magnification.

F. Process Limitations and Yield

The limitations of the process come from the use of optical lithography and contact printing. The use of optical lithography means that the useful range of the UV light source is 350–450 nm. There is a physical limit to the resolution of this light–photoresist system. The best achievable resolution in this wavelength range is 2.5 μm for a 4-μm-thick resist. Contact printing was chosen as the exposure method, because the 52-mm-diameter active area of the mesh dictated a one-to-one mask to image the lithography system. However, putting a resist-coated wafer into contact with the mask generates particulate defects. A noncontact tool such as a proximity printer or a scanning exposure tool would produce fewer defects, although the resolution might suffer. We found that the process had a production yield of ~30% after meshes with obvious defects were removed from the final batch.

3. Results

The goal of this technology development effort was to produce low-absorption, flat, mechanically robust meshes in reasonably large numbers with high precision. To verify that the meshes were uniform and made to specifications, we carried out a series of measurements of linewidth, period, and thickness for comparison with the design parameters. To evaluate the surface smoothness achieved, we obtained phase-interferometry measurements on a sample mesh. Finally we measured the mesh absorption losses to compare with those of commercially available meshes.

A. Mesh Uniformity

We produced meshes with three different sets of linewidth and period design parameters. These specifications are in columns 1 and 2 of Table 1. The design thickness was ~3 μm for all three sets. We measured linewidths and periods, using a scanning electron microscope. Columns 3 and 5 list the linewidths and periods of the masks used to produce the meshes. Columns 4 and 6 list the standard deviation in linewidth and period derived from measurement of these parameters at different positions on a given mask. These numbers provide a measure of the uniformity in the masks. Columns 7 and 10 list the average linewidth and period measured on a set of meshes based on measurements at a number of positions on each mesh in the set. The number of meshes used for these measurements is listed in column 13. Columns 8 and 11 list the average standard deviation (s.d.) obtained for linewidth and period (respectively) measured at a number of positions on a given mesh, providing a measure of the uniformity of the meshes. Columns 9 and 12 list the s.d. of the average mesh linewidth and period obtained for each mesh, providing a measure of the

sample-to-sample variation of the process. From these results it can be seen that both the uniformity and repeatability of the process are good, with somewhat better uniformity achieved in linewidth and smaller sample-to-sample variation achieved in periodicity.

The process linewidths show a widening of ~0.5 μm greater than the mask linewidth. This blooming effect reflects the resolution of the optical lithography. The photoresist thickness of the template, the exposure tool, and the reflectivity of the gold surface all add to the increase of the linewidth. However, all these factors provide a fairly constant widening of the line so that they can be anticipated in the mask design to yield a mesh with the desired linewidth.

We made mesh thickness measurements after process step *d* (see Fig. 2) by a stylus step measuring instrument, as described in Section 2. For example, the group of meshes with a 15.5-μm period had an average thickness of 3.24 μm with a s.d. of 0.42 μm for the set. The average difference between the measurements taken at two positions on the wafer annulus was 0.27 μm.

B. Mesh Flatness

The surface smoothness of the mesh microstructures was evaluated by phase-measurement interferometry. Figure 4 presents the results obtained on a typical mesh measured on a WYKO TOPO-3D[12] phase-measurement interferometer. A plot of the measured mesh topology is shown in Fig. 4(a). The mesh had a thickness of 3.2 μm, a linewidth of 6.1 μm, and a period of 19.2 μm and was fabricated by the ion-milling technique described in Section 2. One can see that, when we average over a region of the mesh, an rms surface smoothness of 13 nm was achieved by this technique with maximum departure from the average surface occurring at the edges of the holes. In Fig. 4(b) we show the surface smoothness measured along the center of a mesh line, which shows approximately an order-of-magnitude improvement.

C. Optical Properties

The far-IR reflectivity and absorption of these meshes were compared with the best commercially available

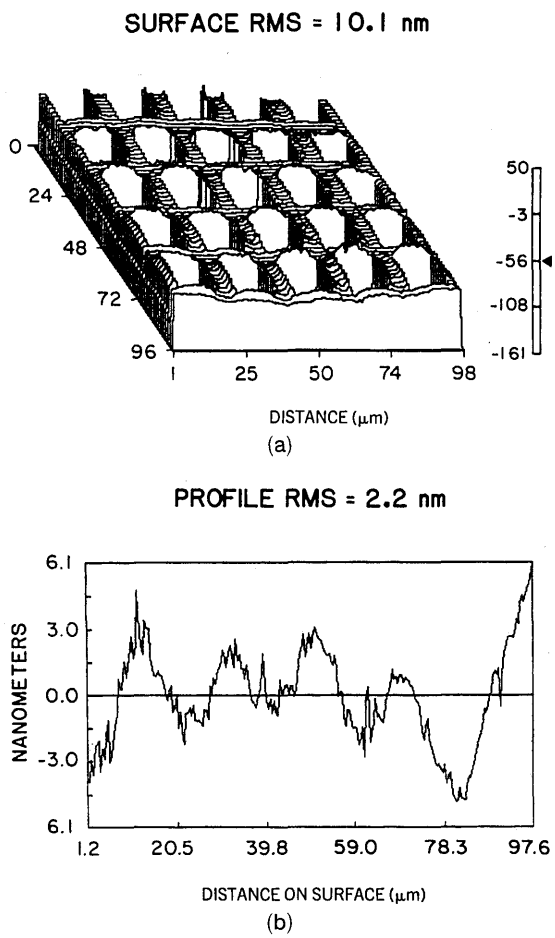

Fig. 4. (a) Plot of typical mesh surface topology measured by optical-phase-measurement interferometry. The typical surface roughness of 13 nm rms is dominated by height deviations at the periphery of the mesh holes. (b) Surface roughness profile of the same mesh, measured along the center of a mesh wire. An order-of-magnitude improvement is revealed when the mesh hole edges are not included in the measurement.

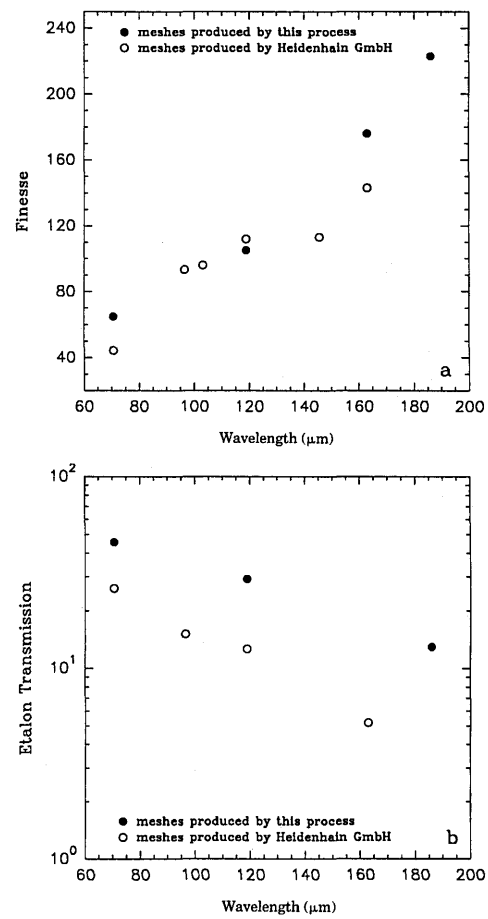

Fig. 5. Plot of finesse and transmission of liquid helium-cooled Fabry–Perot étalons composed of mesh reflectors produced by the process described here and the best commercially available meshes base lined for flight on the ISO.

meshes base-lined for flight on ISO and proposed NASA missions. We formed the meshes into Fabry–Perot étalon plates by stretching them across titanium mounting rings. The Fabry–Perot finesse and étalon transmission were then measured at 4 K on far-IR laser lines. One data set was obtained with meshes mounted in an ISO/long-wavelength spectrometer Fabry–Perot unit and is shown in Fig. 5, reproduced from Greenhouse *et al.*,[7] who discuss the physical behavior of the reflectors.

The results show that meshes produced by this process achieve a factor of 2–10 higher transmission at comparable or higher finesse than other currently available meshes. The measured étalon finesse and transmission indicate mesh absorptivity of 0.7–1.5% with reflectivities of 95–98%. These results are particularly significant in astronomical space-mission applications, for which the background radiation shot noise is below the detector dark current or read noise, and the integration time necessary for one to achieve a required signal-to-noise ratio on faint sources is proportional to the square of the étalon transmission. The mesh reflectors produced by the process described here can significantly increase the scientific mission return of limited lifetime orbital IR observatories.

4. Conclusions

The mesh reflectors produced by the new fabrication process reported here redefine the state of the art for high-finesse, high-transmission, far-IR Fabry–Perot étalons. The additive process approach with template formation and ion-mill finishing is an improvement over previously reported mesh-fabrication processes. Apart from producing meshes that exhibit superior reflectivity and absorption properties, the process reported here affords several advantages: (1) the template process permits fabrication of meshes with linewidths of less than line thickness, extending their applicability to wavelengths as short as 20 μm while maintaining strength for space-flight applications. (2) High-precision geometric tolerance can be achieved over a large area, permitting the mesh performance to be modeled accurately. (3) The process has a higher yield than previously reported processes, which facilitates quantity production.

Testing the meshes shows that they have superior transmission and reflection properties.[7] These results show far-IR mesh reflectivities of 95–98% with corresponding absorption losses of 0.7–1.5%, which is significantly better than that of commercially available meshes.

This research was supported in part by the Office of Naval Research, the Smithsonian Institution, NASA grant NAGW-1711, the Strategic Defense Initiative Office, and a grant from the Max Planck Institut. We thank G. R. Davis and I. Furniss for many useful discussions on mesh requirements for ISO and P. A. R. Ade and G. R. Davis for providing a computer code for modeling the performance of mesh étalons. We thank B. Swinyard and R. Emery for data in advance of publication. We thank G. Windham of the National Security Agency for producing the masks for this project and S. Michel of Commonwealth Science Corporation for assistance with the ion-milling procedure. We also thank the Applied Research Corporation for its participation in the early stages of this program.

References

1. J. M. Vaughn, *The Fabry–Perot Interferometer* (Hilger, Philadelphia, Pa., 1989), Chap. 10, pp. 405–422.
2. B. Carli, "Reflectivity of metallic films in the infrared," J. Opt. Soc. Am. **67,** 908–910 (1977).
3. J. P. Casey and E. A. Lewis, "Interferometer action of a parallel pair of wire gratings," J. Opt. Soc. Am. **42,** 971–977 (1952).
4. K. Sakai and L. Genzel, "Far infrared metal mesh filters and Fabry–Perot interferometry," Rev. Infrared Millimeter Waves **1,** 155–247 (1983).
5. T. De Graauw, "The ISO short wavelength spectrometer," in *Infrared Astronomy with ISO, Proceedings of the Les Houches Summer School,* T. Encrenas and M. F. Kessler, eds. (Nova Science, New York, 1992), pp. 125–138.
6. P. E. Clegg, "The long wavelength spectrometer in ISO," in *Infrared Astronomy with ISO, Proceedings of the Les Houches Summer School,* T. Encrenas and M. F. Kessler, eds., (Nova Science, New York, 1992), pp. 107–122.
7. M. A. Greenhouse, H. A. Smith, J. Fischer, I. Furniss, B. Swinyard, and R. Emery, "Infrared performance characteristics of low-absorption, high-reflectivity metal mesh reflectors," to be submitted to Appl. Opt.
8. C. J. Taylor, H. A. Smith, and J. Fischer, "Superior freestanding meshes for use as infrared Fabry–Perot elements made with a new photolithographic technique," Rev. Sci. Instrum. **59,** 1094–1097 (1988).
9. W. Kern and D. A. Puotinen, "Cleaning solutions based on hydrogen peroxide for use in silicon semiconductor technology," RCA Rev. **31,** 187–206 (1970).
10. H. Smith, F. Bachner, and N. Efrenov, "A high-yield photolithographic technique for surface wave devices," J. Electrochem. Soc. **118,** 821–825 (1971).
11. R. A. Morgan, *Plasma Etching in Semiconductor Fabrication* (Elsevier, New York, 1985), Chap. 2, pp. 40–42.
12. K. N. Prettyjohns and J. C. Wyant, "Three-dimensional surface metrology using a computer controlled noncontact instrument," in *Optics in Engineering Measurement,* W. F. Fagan, ed., Proc. Soc. Photo-Opt. Instrum. Eng. **599,** 304–308 (1986).